

PAPER • OPEN ACCESS

Electronic and optical properties of $\text{InAs}/\text{InAs}_{0.625}\text{Sb}_{0.375}$ superlattices and their application for far-infrared detectors

To cite this article: Ghulam Hussain *et al* 2022 *J. Phys. D: Appl. Phys.* **55** 495301

View the [article online](#) for updates and enhancements.

You may also like






- [Antimonide-based high operating temperature infrared photodetectors and focal plane arrays: a review and outlook](#)
Chunyang Jia, Gongrong Deng, Lining Liu *et al.*
- [Room temperature photoemission up to a wavelength threshold of 2.3 \$\mu\text{m}\$ from \$n^+\$ - \$\text{InAs}_{0.4}\text{P}_{0.6}/\text{p-InAs}_{0.4}\text{P}_{0.6}/\text{p-In}_{0.7}\text{Ga}_{0.3}\text{As}\$ field-assisted photocathode](#)
Minoru Niigaki, Toru Hirohata and Hidenori Mimura
- [Calculation of tunable type-II band alignments in \$\text{InAs}_x\text{Sb}_{1-x}/\text{InAs}\$ heterojunctions](#)
Kyrurhee Shim



ECS
The
Electrochemical
Society
Advancing solid state &
electrochemical science & technology

DISCOVER
how sustainability
intersects with
electrochemistry & solid
state science research

Electronic and optical properties of InAs/InAs_{0.625}Sb_{0.375} superlattices and their application for far-infrared detectors

Ghulam Hussain^{1,*} , Giuseppe Cuono^{1,*} , Rajibul Islam¹ , Artur Trajnerowicz², Jarosław Jureńczyk², Carmine Autieri^{1,3,*}  and Tomasz Dietl^{1,4} 

¹ International Research Centre MagTop, Institute of Physics, Polish Academy of Sciences, Aleja Lotników 32/46, PL-02668 Warsaw, Poland

² VIGO System S.A., 129/133 Poznańska Str., 05-850 Ozarów Mazowiecki, Poland

³ Consiglio Nazionale delle Ricerche CNR-SPIN, UOS Salerno, I-84084 Fisciano (Salerno), Italy

⁴ WPI-Advanced Institute for Materials Research, Tohoku University, Sendai 980-8577, Japan

E-mail: ghussain@magtop.ifpan.edu.pl, gcuono@magtop.ifpan.edu.pl and autieri@magtop.ifpan.edu.pl

Received 1 May 2022, revised 18 September 2022

Accepted for publication 7 October 2022

Published 19 October 2022



Abstract

We calculate the electronic and optical properties of InAs/InAs_{0.625}Sb_{0.375} superlattices (SLs) within relativistic density functional theory. To have a good description of the electronic and optical properties, the modified Becke–Johnson exchange–correlation functional is employed to describe the band gaps correctly. First, we analyze the electronic and optical characteristics of bulk InAs and InSb, and then we investigate the InAs/InAs_{0.625}Sb_{0.375} SL. The optical gaps deduced from the imaginary part of the dielectric function are associated with the characteristic interband transitions. We investigate the electronic and optical properties of the InAs/InAs_{0.625}Sb_{0.375} SL with three lattice constants of the bulk InAs, GaSb and AlSb, respectively. It is observed that the electronic and optical properties strongly depend on the lattice constant. Our results support the presence of two heavy-hole bands with increasing in-plane effective mass as we go far from the Fermi level. We notice a considerable decrease in the energy gaps and the effective masses of the heavy-holes in the k_x – k_y plane compared to the bulk phases of the parent compounds. We demonstrate that the electrons are s -orbitals delocalized in the entire SL, while the holes have mainly p -Sb character localized in the In(As,Sb) side of the SL. In the SL, the low-frequency absorption spectra greatly increase when the electric field is polarized orthogonal to the growth axis allowing the applicability of III–V compounds for the long-wavelength infrared detectors.

* Authors to whom any correspondence should be addressed.



Original Content from this work may be used under the terms of the [Creative Commons Attribution 4.0 licence](https://creativecommons.org/licenses/by/4.0/). Any further distribution of this work must maintain attribution to the author(s) and the title of the work, journal citation and DOI.

Supplementary material for this article is available [online](#)

Keywords: infrared detectors, optical properties, type-II superlattices

(Some figures may appear in colour only in the online journal)

1. Introduction

Over the last few years, InAs/In(As,Sb) Ga- and Hg-free type-II superlattices (T2SLs) have attracted attention as promising candidates for infrared (IR) detector applications due to their narrow gaps and carrier lifetime longer than those in other systems [1–9]. Furthermore, In(As,Sb) quantum wells and nanowires have been proposed as a platform for topological superconductivity [10] while the InAs/GaSb heterostructures host topological states due to their type III band bending [11–13]. Typically, the band structure of these compounds is studied by the envelope function $\mathbf{k} \cdot \mathbf{p}$ formalism or within tight-binding approximation [2]. These empirical methods are successful in describing the conduction band but often fail in the case of the heavy-hole valence band, whose curvature and anisotropy are determined by remote bands not considered usually within effective Hamiltonian methods. In this paper, we determine, by a first-principle method, band structures and optical properties of bulk In(As,Sb) and InAs/InAs_{0.625}Sb_{0.375} SLs with lattice constants of InAs, GaSb and AlSb, respectively. Our results show that the absorption coefficient of SLs is larger than that of bulk materials, reconfirming the superiority of SLs for detector applications. We demonstrate also that the effective mass of heavy-holes in the k_x – k_y plane is much reduced in SLs indicating that III–V SLs might replace IV–VI compounds as efficient Pb-free IR emitters.

The InAs and InSb bulk compounds belong to the family of the III–V zinc-blende semiconductors. For the zinc-blende systems and their alloys, it is possible to grow heterostructures and SLs, in which the alloy content, thickness and interface chemistry can serve to tune the band gap and bandwidths [14] of the two sides of the interface to have type II or type III SL. In a first approximation, in the InAs/In(As,Sb) SLs due to the type II band alignment the electrons are confined within the InAs layer and the holes in the In(As,Sb) layers, and thus electrons and holes are spatially separated. Therefore, by adjustment of the InAs and/or In(As,Sb) thickness as well as the Sb concentration, it is feasible to tune the band gap within a wide range of the IR region. Moreover, the thickness and the Sb concentration have to be tuned to keep the average lattice constant of SL as close as possible to the lattice constant of the substrate. Owing to these unique properties, T2SLs InAs/In(As,Sb) have been chosen as materials for applications in the far-IR radiation. In this paper, we will give more details about the location and dispersion of electrons and holes in T2SLs InAs/In(As,Sb). To achieve this goal, we perform density functional theory (DFT) calculation for a large 3D SL using spin–orbit coupling (SCO) and modified Becke–Johnson (MBJ). On top of this, we calculate the optical properties making this calculation quite computationally demanding. To our knowledge, there was no

previous calculation combining large 3D SL, spin–orbit, MBJ and optical properties.

In section 2, we describe the computational details, section 3 is devoted to the electronic and optical properties of the InAs and InSb bulk while in section 4 the InAs/InAs_{0.625}Sb_{0.375} SL properties are investigated. Finally, section 5 is dedicated to the conclusions.

2. Computational details

We have performed DFT calculations by using the VASP package [15–17]. The core and the valence electrons are treated within the projector augmented wave method [18] with a cutoff of 300 eV for the plane wave basis. Given the importance of SOC in narrow-gap zinc-blende compounds and given the size of the SOC in the elements in question, all calculations have been performed with the relativistic effects taken into account. The valence bands are predominantly composed of anion p -states. Since the SOC energy of p -states is 164 meV in InAs [19], i.e. comparable to the bandgap, the inclusion of SOC is essential for an exact representation of the band structure. If SOC is not included in the calculations, the system is metallic in disagreement with experimental results. For compounds with a zinc-blende structure, DFT within a standard local spin density approximation does not predict properly electronic properties, e.g. band gaps, spin–orbit splittings, and effective masses. The resulting band structure has often a wrong band ordering at the Γ point; these compounds turn out to be zero-gap topological semimetals (like HgTe) rather than narrow-gap semiconductors. Few approaches have made it possible to solve this problem, among these, there is the hybrid exchange–correlation functional [20, 21] and an all-electron screened exchange approach within the full potential linearized augmented plane-wave method [22]. These approaches reproduce the experimental band gaps of these compounds, however, they are computationally expensive to study heterostructures. Therefore, in order to study heterostructures and SLs, we have employed the MBJ exchange–correlation functional together with generalized gradient approximation (GGA) for the exchange–correlation potential [23], which is a semilocal potential that improves the description of the band gaps especially for narrow gap semiconductors [24–26] including zinc-blende semiconductors [21, 27–29]. We can tune the band gap by varying the parameter c^{MBJ} , as reported in supplementary materials figures S1 and S2. The value of c^{MBJ} is the only adjustable parameter that is fixed fitting the band gap of the bulk compounds or the SL. In the literature, the MBJ approach was successfully used for other zinc-blende systems [30]. Despite the MBJ functional having problems with doped systems due to its non-locality [31], we have found that our

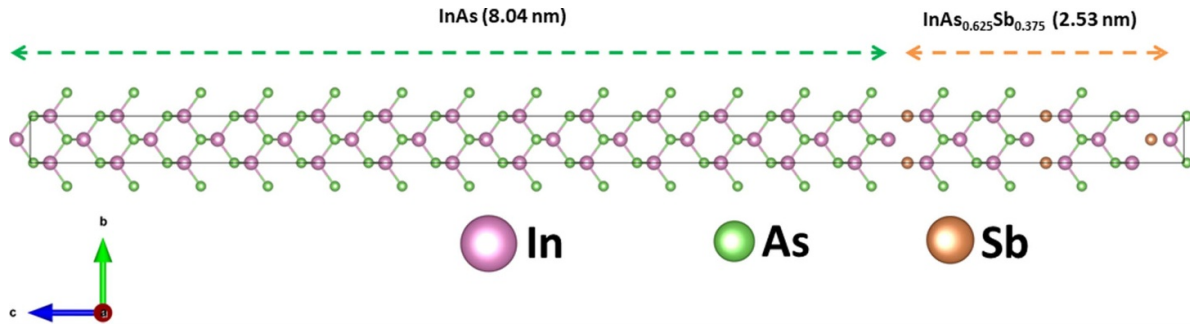


Figure 1. Optimized crystal structure of the InAs/InAs_{0.625}Sb_{0.375} SL grown along the z -axis, (001) axis of the bulk unit cell. The orchid, green and sandy brown spheres represent In, As and Sb atoms, respectively. The dashed green arrow represents the extension of the InAs side of the supercell, while the dashed orange arrow represents the extension of the InAs_{0.625}Sb_{0.375} side of the superlattice. The solid black line represents the unit cell of the superlattice.

results for the bulk system are quite remarkable. Therefore, we conclude that the MBJ provides reliable results if the properties of the doping do not differ too much from the properties of the host as in the case InAs doped with Sb. The GGA+U does not solve the gap problem for the zinc-blende unless we would use exotic negative Coulomb repulsions [32].

To inspect how the energy gaps and optical properties of InAs/InAs_{0.625}Sb_{0.375} SL change as a function of the lattice constant, we used room temperature lattice constants of InAs, GaSb and AlSb, respectively. The values of the lattice parameters at $T = 300$ K are: $a_{\text{InAs}} = 6.0583$ Å, $a_{\text{GaSb}} = 6.0959$ Å and $a_{\text{AlSb}} = 6.1355$ Å [33]. In other words, we considered the SL is grown on InAs, GaSb and AlSb substrates, respectively. The SLs are treated as fully strained and we have a perfect interface without intermixing. Our (001) SL is composed of 8.04 nm of InAs (26 unit cells) and 2.53 nm of InAs_{5/8}Sb_{3/8} (8 unit cells), as shown in figure 1.

3. Bulk properties

In this section, we investigate the electronic and optical properties of the InAs and InSb bulk to use as a benchmark for the investigation on the SL.

3.1. Electronic properties of the InAs and InSb bulk

Using the eigenvalues at the Γ point of InAs and InSb bulk, we can calculate the band bending of the SLs. The band bending of the InAs/InSb returns a type III SL, while the band bending of the InAs/InAs_{0.625}Sb_{0.375} returns a type II SL in agreement with experimental data. For the calculation of band gap of InAs_{0.625}Sb_{0.375}, we have used the virtual crystal approximation for the energetic levels with $0.625E_{c,v;\text{InAs}} + 0.375E_{c,v;\text{InSb}}$ where $E_{c,v;\text{InAs}}$ and $E_{c,v;\text{InSb}}$ are the energetic levels of the valence (v) or conduction (c) bands of InAs and InSb, respectively. This highlights how our computational setup is reliable in the description of the electronic properties of this material class.

Using the notation of [20], table 1 summarizes the effective masses of the energy bands such as $m_{\text{split-off}}$, $m_{\text{light-hole}}$, $m_{\text{heavy-hole}}$ and conduction electron m_{electron} along the directions [100], [110] and [111] for various theoretical

Table 1. Effective masses of bulk InAs calculate within MBJ (this work) compared with other theoretical approaches [20] and experimental results [34, 35] at Γ along different directions of the k -space. Increasing the energy, we name the bands as split-off, light-hole, heavy-hole and electron bands as used in the literature [20].

Approach	Direction	$m_{\text{split-off}}$	$m_{\text{light-hole}}$	$m_{\text{heavy-hole}}$	m_{electron}
HSE06	[100]	0.112	0.033	0.343	0.027
	[111]	0.111	0.031	0.836	0.027
	[110]	0.112	0.032	0.623	0.027
MBJ	[100]	0.189	0.064	0.155	0.021
	[111]	0.119	0.046	0.609	0.014
	[110]	0.062	0.037	0.409	0.031
Experiment	[100]	0.140	0.027	0.333	0.023
	[111]	0.140	0.037	0.625	0.026
	[110]	0.140	0.026	0.410	0.026

and experimental approaches. In this paper, we have fitted the DFT band structure with a quadratic dispersion and reported the numerical values of the fitting. The effective masses calculated for heavy-hole along the [111] and [110] directions strongly match experimental results. Similarly, the effective masses of conduction electrons in the [100] and [111] directions coincide with those of experiments. Respect to the Heyd–Scuseria–Ernzerhof (HSE06) exchange-correlation results present in the literature, the light-holes in MBJ are heavier than HSE06 while the heavy-holes in MBJ are lighter than HSE06.

3.2. Optical properties of the InAs and InSb bulk

The optical properties of a particular semiconductor are of great interest due to their possible applications in optoelectronics and photon sensing. After establishing the values of c^{MBJ} for the bulk compounds, as reported in the supplementary materials figures S1 and S2, we calculate the optical properties of InAs and InSb at $T = 0$. In figures 2 and 3 we show optical characteristics of InAs and InSb in the bulk form, respectively. Due to the cubic symmetry, the optical properties of InAs and InSb bulk are isotropic and therefore independent on whether the electric field is polarized along the x -, y - and z -axis.

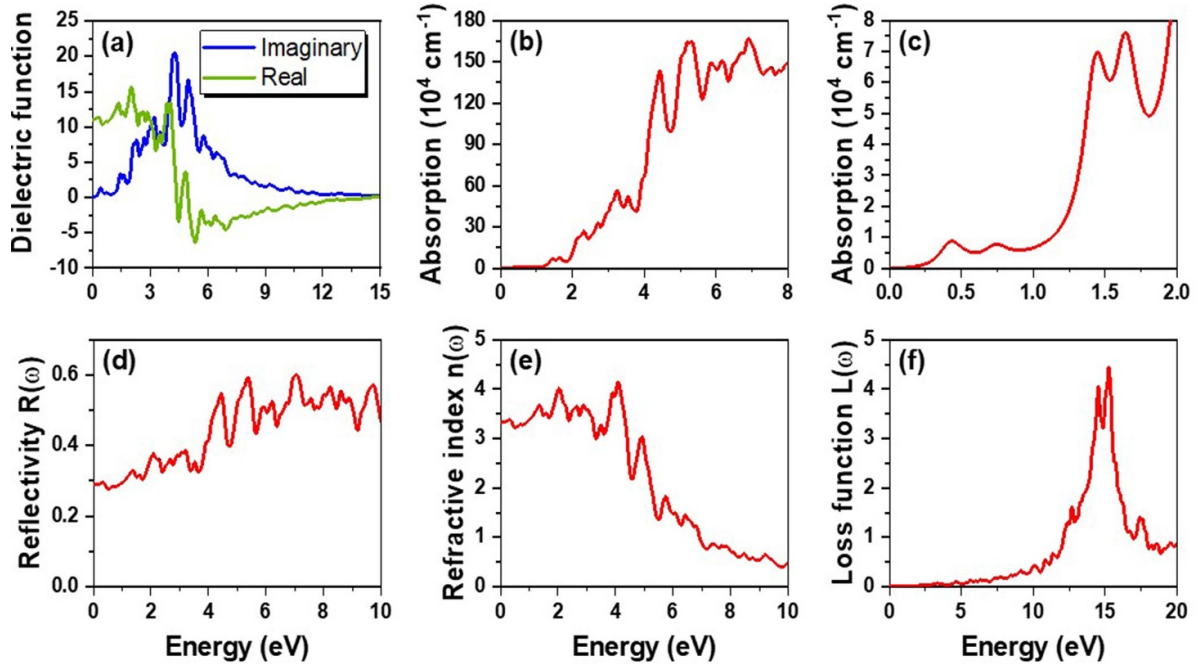


Figure 2. Frequency-dependent optical properties of InAs bulk with the low-temperature lattice constant. (a) Real (green line) and imaginary (blue line) parts of the dielectric function. (b) Absorption spectrum in the frequency-range between 0 and 8 eV. (c) Absorption spectrum in the IR region. (d) Reflectivity. (e) Refractive index. (f) Energy loss function.

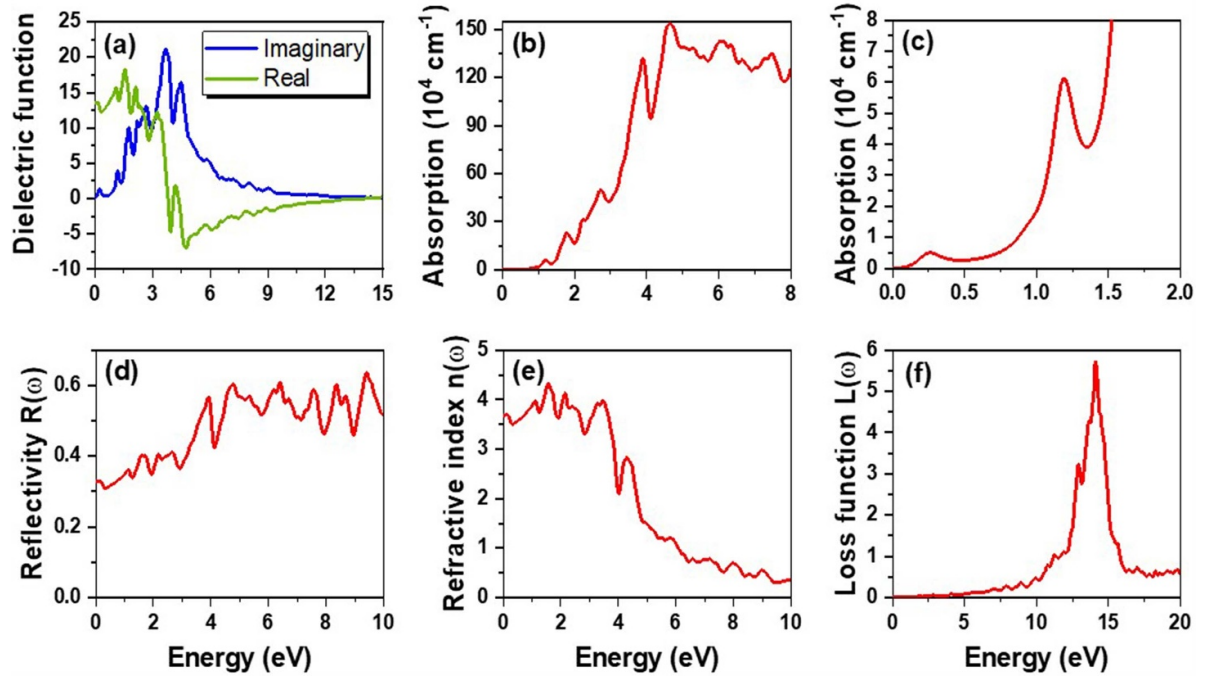


Figure 3. Frequency-dependent optical properties of InSb bulk with the low-temperature lattice constant. (a) Real (green line) and imaginary (blue line) parts of the dielectric function. (b) Absorption spectrum in the frequency-range between 0 and 8 eV. (c) Absorption spectrum in the IR region. (d) Reflectivity. (e) Refractive index. (f) Energy loss function.

Figures 2(a) and 3(a) illustrate the real and imaginary parts of the dielectric function for InAs and InSb, which are used to extract other optical responses for the system. The values of the real part of the dielectric function on the vertical y-axis of the graph are known as static values of the real part; the value of static dielectric constant for InAs is 11.07, while that of InSb

is 13.42, which is in agreement with the values reported in theoretical [36, 38] and experimental works [37]. Table 2 gives a comparison between the present work and the literature. The imaginary and real parts of the dielectric function [39], as well as the refractive index, are in very good agreement with the literature [39] for both InAs and InSb.

Table 2. Static dielectric constants (ϵ) and refractive indices (n_0) for the InAs bulk in the present work and in the literature.

Approach	ϵ	(n_0)
Present work	11.07	3.315
GGA-EV theory [36]	10.82	3.289
Experiment [37]	11.67	—

If we look at the absorption spectra of figures 2(b) and 3(b), we can see that the first absorption peaks appear at 0.417 eV for InAs and 0.235 eV for InSb. These peaks correspond to the energy-gap between the highest occupied and the lowest unoccupied energy bands, characterizing specific electronic transitions. In figures 2(c) and 3(c) we zoom in the 0–2 eV energy range, to quantify and describe the importance of InAs and InSb semiconductors in the IR region. Previous calculations on the same material class were reported using an all-electron method with c^{MBJ} calculated self-consistently [40, 41] and tight-binding method [42], despite the different methodology our results are in quantitative agreement with the theoretical literature. If we compare our absorption spectra with experimental literature, we find that our theoretical absorption coefficients overestimate the experimental values as expected neglecting the local field effect.

Besides, the surface behavior of these semiconductors is studied via reflectivity, which is defined as the ratio of the reflected and incident power. Figures 2(d) and 3(d) display the reflectivity spectra for InAs and InSb, which indicate that these compounds are less reflective in the IR region compared to other regions. Nevertheless, the refractive index shows a substantial value in the IR region, as we can see from figures 2(e) and 3(e). The low reflectivity and higher refractive index in the IR region make these materials very useful for IR detectors. The static refractive indices n_0 are 3.315 and 3.684 for InAs and InSb, respectively. Further, the energy loss function (ELF) is calculated in figures 2(f) and 3(f), to measure the loss of energy taking place in the systems. Almost no energy loss can be seen for the photons in the IR region. However, as the energy increases beyond 5 eV, energy loss starts to increase and becomes maximum around 15 eV. The peaks in ELF spectra correspond to the plasma resonance and hence the associated frequency is the plasma frequency.

4. Study of the InAs/InAs_{0.625}Sb_{0.375} SL

In this section, we study the SL of InAs/InAs_{0.625}Sb_{0.375} since it is employed in the devices of IR-detectors. Here, we use as in-plane lattice constant of the SL the values of the InAs, GaSb and AlSb at $T = 300$ K, respectively [33]. We used the value of $c^{\text{MBJ}} = 1.22$ for all atoms of the SL. This value gives a reasonable agreement with experimental results of 0.1 eV [43]. Then, we calculated the band structures and optical properties of the SL for the three different lattice constants. Both InAs and InSb have the zinc-blende as a structural ground state, then we do not expect any structural disorder in the alloy part of the SL. The following two subsections present the electronic and optical attributes with these three lattice constants.

4.1. Electronic properties of the SL

After the structural relaxation of the InAs/InAs_{0.625}Sb_{0.375} SL, the electronic properties were calculated. Figure 4 shows the band structures calculated along the \mathbf{k} -path X- Γ -M-X for the InAs/InAs_{0.625}Sb_{0.375} SL for the three lattice constants of bulk InAs, GaSb and AlSb, sequentially. We noticed a considerable decrease in the energy gaps compared to the parent compounds which allows their applicability in far-IR detection. The value of the band gap is calculated to be 116 meV in the case of a_{InAs} , while for a_{GaSb} this decreases to 87 meV and further decreases to 53 meV for a_{AlSb} , as shown in table 3. We noticed that, as the value of the lattice constant increases, the energy gap of the SL decreases.

At the Γ point below the Fermi level, we have the highest valence band (HVB) two times degenerate. At 0.1 eV below HVB, we find another hole band two times degenerate, and another hole band two times degenerate at 0.25 eV below the HVB. All these six bands become almost degenerate at the high-symmetry point X, therefore, all these bands originate from the heavy-holes and light-holes of the bulk. We define the two HVBs as heavy-holes and the third highest valence band as light-hole. The presence of multiple heavy-hole bands is a huge difference respect to the bulk. The number of heavy-holes bands strongly depends on the period of the SL [43, 44]. In the literature with tight-binding models, usually it was reported one heavy-hole band [42, 43] for a 10.57 nm period. However, within first-principle calculations, we obtained two heavy-hole bands. The far we go from the Fermi level, heavier the effective masses of these bands become as opposite to the bulk where we have the HVB as heavy-hole and the second HVB as light-hole. In the case of the SL, we define the HVB as heavy-hole1 and the second HVB as heavy-hole2. To study the effect of lattice constant on the effective masses of the charge carriers, we computed the effective masses at the Γ point of the SL such as $m_{\text{heavy-hole2}}$, $m_{\text{heavy-hole1}}$ and m_{electron} along the two in-plane directions i.e. [100] and [110] as shown in table 3. We report different effective masses for the [100] and [110] directions, going beyond the approximation of isotropic effective mass in the k_x - k_y plane found in the literature.

Due to the change of the symmetry, it is not possible to compare directly the effective masses along the same directions in bulk and SL. However, it is interesting to compare the effective masses of the SL respect to the effective masses of the bulk, since we expect that this trend can be observable in experiments. The biggest change in the SL is the reduction of the effective masses of the HVB (heavy-hole1) respect to the bulk, while the second HVB (heavy-hole2) is now heavier as opposite to the bulk. The effective masses that we have calculated are in line with previous effective masses calculated with other theories [42, 43, 45]. A considerable decrease of the effective masses along the [100] direction can be seen, as the lattice constant increases from 6.05 830 Å (InAs) to 6.1355 Å (AlSb). Except for the m_{electron} , the effective masses along the [110] direction are smaller than the effective masses along the [100] direction. We have noticed that the lattice constant not only influences the band gaps but also the effective masses associated with charge carriers. Indeed, except for the m_{electron} ,

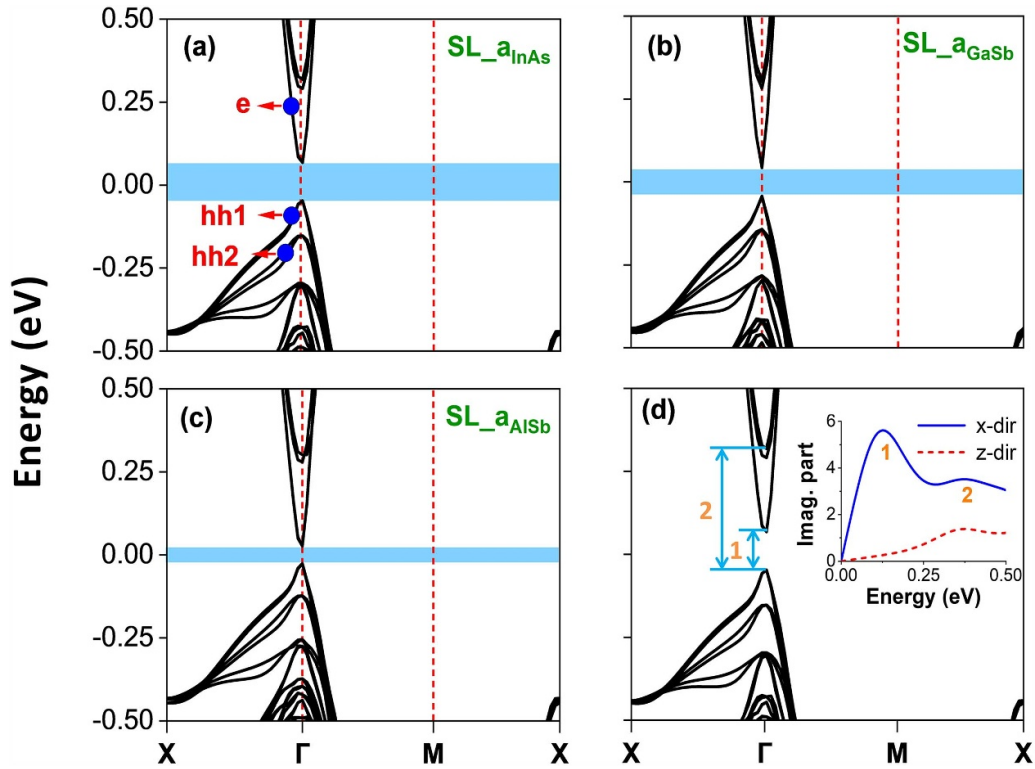


Figure 4. Band structures of the SL for three different lattice constants at 300 K i.e. (a) a_{InAs} , (b) a_{GaSb} and (c) a_{AlSb} . (d) Numbers 1 and 2 indicate the characteristic interband transitions. The inset shows the peaks associated with the number 1 and 2 in the imaginary part of the dielectric function for the x- and z-polarization of the electric field. The Fermi level is set to zero.

Table 3. Effective masses of InAs/InAs_{0.625}Sb_{0.375} at Γ point along in-plane directions of the k -space for the lattice constants of InAs, GaSb and AlSb and their comparison with the literature [43].

Lattice constant (\AA)	Band gap	Direction	$m_{\text{light-hole}}$	$m_{\text{heavy-hole2}}$	$m_{\text{heavy-hole1}}$	m_{electron}
InAs (6.0583)	0.116 eV	[100]		0.196	0.175	0.022
		[110]		0.062	0.056	0.023
GaSb (6.0959)	0.087 eV	[100]		0.147	0.126	0.016
		[110]		0.052	0.041	0.018
AlSb (6.1355)	0.053 eV	[100]		0.112	0.099	0.016
		[110]		0.046	0.044	0.024
k-p model for 14.5 nm SL [43]	0.1 eV	k_x - k_y plane	0.096		0.040	0.019
InAs/GaSb with 17 layers [44]	0.1 eV	k_x - k_y plane	0.051–0.061		0.33–0.37	0.023–0.031

Table 4. Effective masses of InAs/InAs_{0.625}Sb_{0.375} at Γ point along k_z for the lattice constants of InAs, GaSb and AlSb and their comparison with the literature [43].

Lattice constant (\AA)	Band gap	Direction	$m_{\text{light-hole}}$	$m_{\text{heavy-hole1}}$	$m_{\text{heavy-hole2}}$	m_{electron}
GaSb (6.0959)	0.087 eV	[001]		54.9	32.5	0.256
k-p model for 14.5 nm SL [43]	0.1 eV	[001]	0.104		31.02	0.023

the effective masses decrease with the increase of the lattice constant of the SL.

The SL Brillouin zone is very different from the bulk Brillouin zone due to the change of the unit cell symmetries and lattice constants. In particular, the z-axis is extremely elongated flattening the band and increasing the effective mass along the [001] direction [43]. The calculated effective masses along [001] are reported in table 4 and compared with the

literature. The calculated effective masses of the heavy-holes along [001] are extremely high as 54.9 which is comparable with the literature. The effective electron mass along [001] is 0.256 which is one order of magnitude larger than the in-plane effective masses. The reason for the difference between holes and electrons lies in the properties of the Γ_6 in zinc-blende semiconductors. The wave function of the Γ_6 state is in a quantum bonding state between the s-orbitals of Indium that

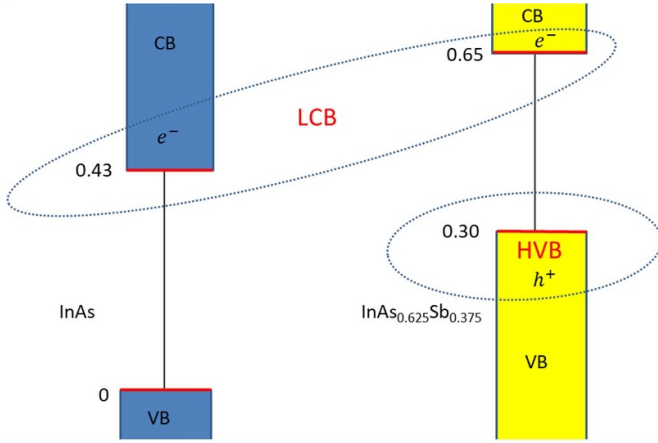


Figure 5. Type-II band bending using the gap of bulk InAs and $\text{InAs}_{0.625}\text{Sb}_{0.375}$ calculated for $c^{\text{MBJ}} = 1.180$. From the bulk data, we estimate the LCB and HVB of the supercell. The filled rectangulars represent the electronic bands connected by black lines representing the band gap. e^- and h^+ represent electrons and holes. The ovals represent the positions of LCB and HVB in the real space, while the HVB is mainly located in the $\text{In}(\text{As},\text{Sb})$ side, the electrons are delocalized along the superlattice. The energy zero is fixed at the top of the valence band of InAs. The numerical values are in eV.

can be approximated as: $|\Gamma_6\rangle \approx \frac{1}{\sqrt{N}} \sum_{i=1,N} |5s\text{-In}_i\rangle$ where the index i runs on the N atoms of Indium present in the supercell, minor contributions from the s orbitals of the anions are also present. This bonding state is delocalized on both sides of the supercell. The band bending of the T2SL $\text{InAs}/\text{InAs}_{0.625}\text{Sb}_{0.375}$ is shown in figure 5 together with the atomic character of the electrons of the lowest conduction band (LCB) and HVB of the $\text{InAs}/\text{InAs}_{0.625}\text{Sb}_{0.375}$ supercell. The DFT results confirm that the orbital character of the LCB is mainly $5s\text{-In}$ while the orbital character of the HVB is mainly $5p\text{-Sb}$. In summary, the electrons are delocalized along the SL owning a small mass, while the holes are localized in the $\text{In}(\text{As},\text{Sb})$ side of the SL owning a huge effective mass. As a consequence the concentration and the distribution of the Sb doping mainly affects the hole carriers. The gap obtained from the band bending is 0.13 eV, which is in agreement with the literature [46] and in qualitative agreement with the more accurate results for the supercell presented in table 3.

In figure 4(d), the interband electronic transitions related to the excitations in the SL are described. The light–matter interactions can be explained by the complex dielectric function, i.e. the imaginary part is directly linked to the absorption. The observed peaks in the inset of figure 4(d) can be connected to the excitation of electrons from the valence band maximum to the conduction bands for a_{InAs} based SL, which are also indicated by the interband transitions in figure 4(d) with the transition number 1 at 115 meV and with the transition number 2 at 365 meV. These excitations can take place owing to the vertical transition from the valence band to the conduction bands at the Γ point of the Brillouin zone as indicated in figure 4(d). Since the gap depends on the lattice constant, we figured out that also the energies required to cause the interband transitions are affected by the different lattice constants.

4.2. Optical properties of the SL

Based on the relaxed structure, we have explored the optical properties of $\text{InAs}/\text{InAs}_{0.625}\text{Sb}_{0.375}$ SLs with the MBJ exchange-correlation functional. Again, the three different lattice constants are considered to calculate the optical properties as illustrated in figures 6, S3 and S4, respectively. For the SL, we observed that all the optical properties are anisotropic because of the reduction in symmetry [47]. Besides, the results in figures 6(a), S3 and S4 are almost identical, which shows that the small changes in in-plane lattice constant has a very small effect on the optical properties. Figures 6(a), S3(a) and S4(a) demonstrate the real and imaginary parts of the dielectric function for the three cases, respectively. Owing to the anisotropy, the values of static dielectric constants for SLs with the InAs, GaSb and AlSb lattice constant are (19.40, 15.57), (24.06, 12.20) and (30.00, 13.14) in the x and z -directions, respectively. Table 5 demonstrates the static dielectric constants (ϵ_x, ϵ_z) and refractive indices (n_x, n_z) of $\text{InAs}/\text{InAs}_{0.625}\text{Sb}_{0.375}$ for lattice constants of InAs, GaSb and AlSb, respectively. The absorption coefficients of the SL for the three lattice constants are shown in figures 6(b), (c), S3(b), (c) and S4(b), (c). The first absorption peak appears near 0.115 eV and the second appears at 0.365 eV in the case of InAs lattice constant, for the GaSb case they appear at 0.092 eV and 0.316 eV while for the AlSb case the first and second peaks appear at 0.082 eV and 0.273 eV, respectively.

In figures 6(b), S3(b) and S4(b), we report the absorption spectra in the region between 0 and 8 eV. The absorption spectra strongly increase from the frequency of the energy gap until approximately 5 eV. Beyond 5 eV, the absorption spectrum reaches a plateau with moderate oscillations of the order of 15%. Including the electron–hole interaction, the plateau would be reached at lower frequencies. Similarly in figures 6(c), S3(c) and S4(c), we report the absorption spectra in the region between 0 and 2 eV that is the relevant region for IR detectors. We report the absorption coefficient when the electric field is polarized along the x -axis (α_{E_x}) and z -axis (α_{E_z}). We can immediately see how the absorption coefficient is much larger when the electric field is polarized along the x -axis, i.e. orthogonal to the growth axis. Defining θ as the angle between the polarization of the electric field and the z -axis, we have that the absorption coefficient $\alpha(\theta)$ is equal to:

$$\alpha(\theta) = \sin(\theta)\alpha_{E_x} + \cos(\theta)\alpha_{E_z}. \quad (1)$$

We have found characteristic absorption peaks in the low-energy regions that quantify the characteristic interband transitions. This employs the possibility of using these SLs for IR detection. Similar to the bulk case, the SL is also less reflective in the IR region (see figures 6(d), S3(d) and S4(d)). Also, the refractive indices are higher in the IR range as shown in figures 6(e), S3(e) and S4(e). Such less reflection of the photons and higher corresponding indices of refraction in the IR range of the electromagnetic spectrum suggests their applications in the IR detectors. It can be noticed that the static refractive indices n_0 are also anisotropic; these are (4.4, 3.4), (4.9, 3.5) and (5.5, 3.6) for InAs, GaSb and AlSb based lattice constants in the (x, z) directions (table 5). Moreover, the ELF's

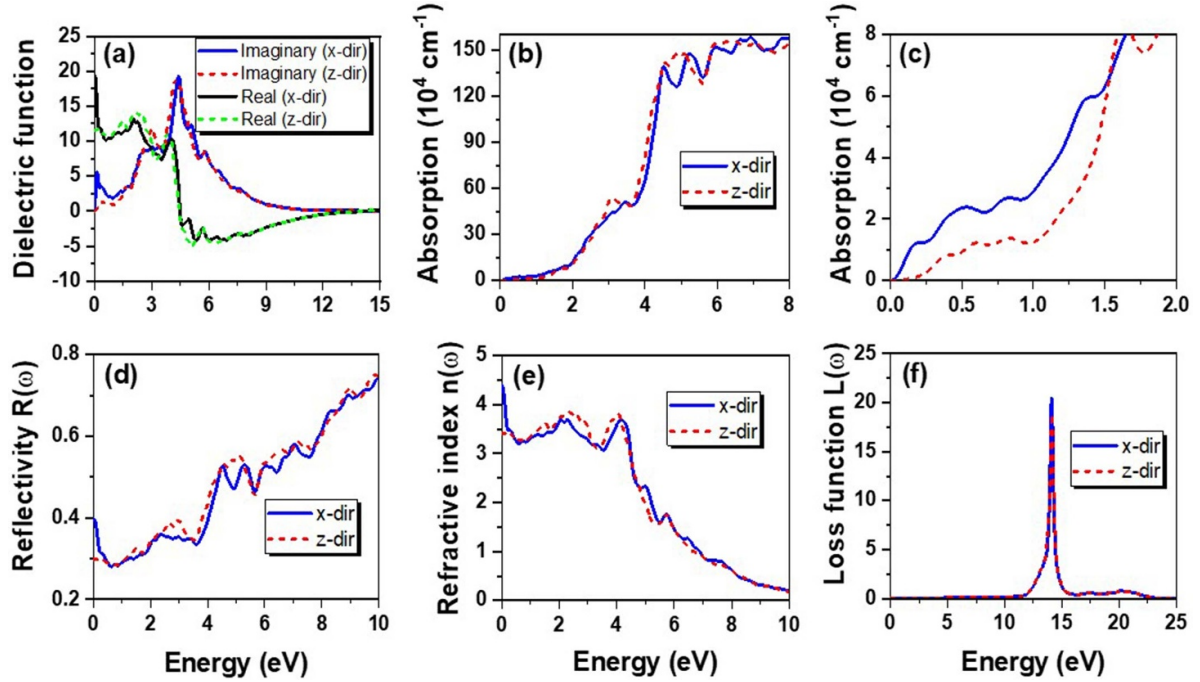


Figure 6. Frequency-dependent optical properties of InAs/InAs_{0.625}Sb_{0.375} superlattice with lattice constant at $T = 300$ K that is $a_{\text{InAs}} = 6.0583$ Å. (a) Real and imaginary parts of the dielectric function. (b) Absorption spectra in the frequency-range between 0 and 8 eV. (c) Absorption spectra in the IR region. (d) Reflectivity. (e) Refractive index. (f) Energy loss function. The x-dir and z-dir indicate the directions of the electric field polarized perpendicular and parallel to z-axis of the SL.

Table 5. Static dielectric constants (ϵ_x, ϵ_z) and refractive indices (n_x, n_z) of InAs/InAs_{0.625}Sb_{0.375} for lattice constants of InAs, GaSb and AlSb, respectively, using the MBJ approach.

Lattice constant (Å)	ϵ_x	ϵ_z	n_x	n_z
InAs (6.0583)	19.4	15.6	4.40	3.40
GaSb (6.0959)	24.1	12.2	4.90	3.51
AlSb (6.1355)	30.0	13.1	5.51	3.60

for the three cases reveal almost identical behavior and show no energy loss up to 12 eV, particularly for the photons in the IR range as shown in figures 6(f), S3(f) and S4(f).

Since the most relevant physical property for the far-IR detectors is the absorption spectrum, finally, we compare the absorption spectra in the IR region for InAs bulk and the SLs in figure 7. It can be seen that the absorption strongly increases for SL in the IR regime as compared to InAs bulk. Also, the absorption is observed to increase as a function of the lattice constant and becomes maximum for the lattice constant of a_{AlSb} . The reason for the large absorption coefficient of the SL could be attributed to the presence of the two heavy-hole bands. Then, we can speculate that thicker SLs could produce even larger absorption spectra provided that the quality of the sample and the strain would be uniform along the SL. However, the uniform strain is limited by the critical thickness in the experimental realization.

To go beyond the independent-particle approximation employed here for the optical properties, we would need the using Bethe–Salpeter equation that includes the electron–hole interaction. The Bethe–Salpeter equation would produce a

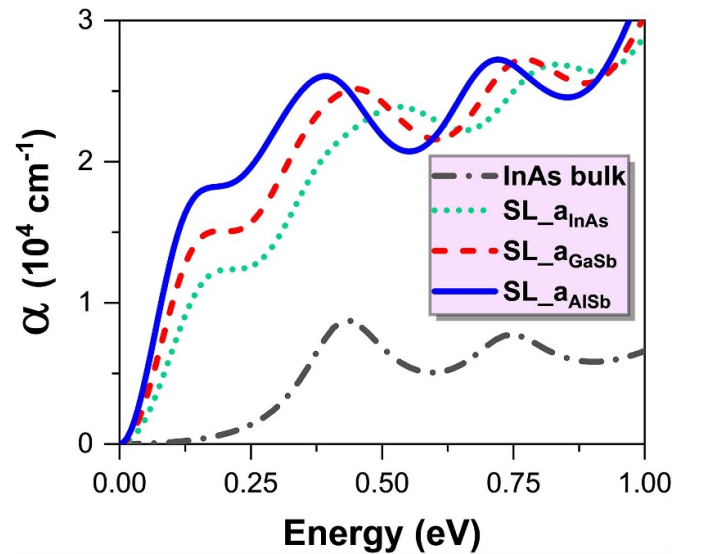


Figure 7. Absorption coefficient for an electric field polarized along the x-direction in the far-infrared regime between 0 and 1 eV. Spectra of InAs bulk (dash-dotted grey line) and InAs/InAs_{0.625}Sb_{0.375} SLs for InAs (dotted green line), GaSb (dashed red line) and AlSb (solid blue line) substrate.

shift of the peak in the imaginary part to lower frequencies [48, 49]. The Bethe–Salpeter couples the electron and the hole, and thus takes into account the electron–hole interactions [50]. This approach has been very successful for the calculation of absorption spectra of a large variety of systems bearing large band gaps, such as wide band gap semiconductors

and insulators [51]. On the other hand, the small-gap semiconductors and metals, instead, screen this electron–hole interaction, and the resulting contribution can therefore be negligible. Since we are dealing with ultranarrow gap semiconductors, the MBJ potential is sufficient for our study.

5. Conclusions and outlook

We have investigated the electronic and optical properties of InAs and InSb bulk and their SLs. We perform a computationally demanding calculation for the realistic system combining a large SL, SCO, MBJ and optical properties. We focus on the InAs/InAs_{0.625}Sb_{0.375} SL with the three lattice constants of the bulk InAs, GaSb and AlSb, respectively. It is observed that the electronic and optical properties effectively change due to the different symmetry present in the SL and with the lattice constant of the SL. In the SL, we notice a considerable decrease in both the energy gaps and the effective masses of the heavy-holes compared to the bulk phases of the parent compounds. As opposite to the tight-binding literature, we have found two heavy-hole bands with the in-plane effective mass increasing as far as we go further from the Fermi level. In the k_x – k_y plane, the effective masses of the heavy-holes in the SL become comparable with the one of the light-holes of the bulk. Along the growth axis, the effective mass of the hole becomes huge while the effective mass of electron increases less significantly. This happens since the electrons are delocalized in the entire SL while the holes are localized in the In(As,Sb) side of the SL. As future prospects, it would be helpful to simulate the randomness of the Sb distribution and the possible Sb interdiffusion in the InAs layer. This would require larger supercells and could not be done following this computational approach.

Our theoretical calculations demonstrate that the absorption spectra in the far-IR regime strongly increased in the case of SL with respect to bulk InAs and InSb. The absorption coefficient of the SL is larger if the electric field is polarized in the direction orthogonal to the growth axis. Moreover, the absorption spectrum as a function of the lattice constant is increased at low frequency. The appearance of multiple heavy-hole and a small energy gaps of the order of meVs produces a high absorption coefficient making these SLs employable for applications in far IR detectors. The large sensitivity of the optical properties to structural and chemical degrees of freedom opens the possibility of engineering the optical property of the InAs-based SL making them even more appealing for the construction of far IR detectors.

Data availability statement

The data that support the findings of this study are available upon reasonable request from the authors.

Acknowledgments

G H and G C contributed equally to this work. We thank T Story and M Birowska for useful discussions. The work is supported by the Foundation for Polish Science through the

International Research Agendas program co-financed by the European Union within the Smart Growth Operational Programme. This work was financially supported by the National Science Center in the framework of the ‘PRELUDIUM’ (Decision No.: DEC-2020/37/N/ST3/02338). We acknowledge the access to the computing facilities of the Interdisciplinary Center of Modeling at the University of Warsaw, Grants G84-0, GB84-1 and GB84-7. We acknowledge the CINECA award under the ISCRA initiative IsC85 ‘TOPMOST’ and IsC93 ‘RATIO’ grant, for the availability of high-performance computing resources and support.

ORCID iDs

Ghulam Hussain  <https://orcid.org/0000-0003-1654-9156>
 Giuseppe Cuono  <https://orcid.org/0000-0002-1550-5429>
 Rajibul Islam  <https://orcid.org/0000-0001-9076-7843>
 Carmine Autieri  <https://orcid.org/0000-0002-5008-8165>
 Tomasz Dietl  <https://orcid.org/0000-0003-1090-4380>

References

- [1] Rogalski A, Martyniuk P and Kopytko M 2017 InAs/GaSb type-II superlattice infrared detectors: future prospect *Appl. Phys. Rev.* **4** 031304
- [2] Rogalski A, Martyniuk P, Kopytko M, Madejczyk P and Krishna S 2020 InAsSb-based infrared photodetectors: thirty years later on *Sensors* **20** 24
- [3] Ting D Z, Rafol S B, Khoshakhlagh A, Soibel A, Keo S A, Fisher A M, Pepper B J, Hill C J and Gunapala S D 2020 InAs/InAsSb type-II strained-layer superlattice infrared photodetectors *Micromachines* **11** 11
- [4] Ting D Z, Khoshakhlagh A, Soibel A and Gunapala S D 2020 Long wavelength InAs/InAsSb infrared superlattice challenges: a theoretical investigation *J. Electron. Mater.* **49** 6936–45
- [5] Martyniuk P, Michalczewski K, Tsai T Y, Wu C and Wu Y R 2020 Theoretical modeling of XBn T2SLs InAs/InAsSb/B-AlSb longwave infrared detector operating under thermoelectrical cooling *Opt. Quantum Electron.* **52** 6936–45
- [6] Ting D Z, Soibel A, Khoshakhlagh A, Keo S A, Rafol S B, Fisher A M, Pepper B J, Luong E M, Hill C J and Gunapala S D 2019 Advances in III–V semiconductor infrared absorbers and detectors *Infrared Phys. Technol.* **97** 210–6
- [7] Wu D, Durlin Q, Dehzangi A, Zhang Y and Razeghi M 2019 High quantum efficiency mid-wavelength infrared type-II InAs/InAs_{1–x}Sb_x superlattice photodiodes grown by metal-organic chemical vapor deposition *Appl. Phys. Lett.* **114** 1
- [8] Steenbergen E H *et al* 2011 Significantly improved minority carrier lifetime observed in a long-wavelength infrared III–V type-II superlattice comprised of InAs/InAsSb *Appl. Phys. Lett.* **99** 251110
- [9] Klipstein P C, Livneh Y, Glozman A, Grossman S, Klin O, Snapi N and Weiss E 2014 Modeling InAs/GaSb and InAs/InAsSb superlattice infrared detectors *J. Electron. Mater.* **43** 8
- [10] Moehle C M *et al* 2021 InSbAs two-dimensional electron gases as a platform for topological superconductivity *Nano Lett.* **21** 9990–6

- [11] Pikulin D I and Hyart T 2014 Interplay of exciton condensation and the quantum spin Hall effect in InAs/GaSb bilayers *Phys. Rev. Lett.* **112** 176403
- [12] Winkler G W, Wu Q, Troyer M, Krogstrup P and Soluyanov A A 2016 Topological phases in InAs_{1-x}Sb_x: from novel topological semimetal to Majorana wire *Phys. Rev. Lett.* **117** 076403
- [13] Nguyen N M, Cuono G, Islam R, Autieri C, Hyart T and Brzezicki W 2022 Unprotected edge modes in quantum spin Hall insulator candidate materials (arXiv:2209.06912)
- [14] Mikhailova M P, Moiseev K D and Yakovlev Y P 2004 Interface-induced optical and transport phenomena in type II broken-gap single heterojunctions *Semicond. Sci. Technol.* **19** R109–28
- [15] Kresse G and Hafner J 1993 *Ab initio* molecular dynamics for liquid metals *Phys. Rev. B* **47** 558–61
- [16] Kresse G and Furthmüller J 1996 Efficiency of *ab-initio* total energy calculations for metals and semiconductors using a plane-wave basis set *Comput. Mater. Sci.* **6** 15–50
- [17] Kresse G and Furthmüller J 1996 Efficient iterative schemes for *ab initio* total-energy calculations using a plane-wave basis set *Phys. Rev. B* **54** 11169–86
- [18] Kresse G and Joubert D 1999 From ultrasoft pseudopotentials to the projector augmented-wave method *Phys. Rev. B* **59** 1758–75
- [19] Cuono G, Autieri C, Guarnaccia G, Avella A, Cuoco M, Forte F and Noce C 2019 Spin–orbit coupling effects on the electronic properties of the pressure-induced superconductor CrAs *Eur. Phys. J. Spec. Top.* **228** 631–41
- [20] Kim Y-S, Hummer K and Kresse G 2009 Accurate band structures and effective masses for InP, InAs and InSb using hybrid functionals *Phys. Rev. B* **80** 035203
- [21] Cuono G, Autieri C and Dietl T 2022 In manuscript
- [22] Geller C B, Wolf W, Picozzi S, Continenza A, Asahi R, Mannstadt W, Freeman A J and Wimmer E 2001 Computational band-structure engineering of III–V semiconductor alloys *Appl. Phys. Lett.* **79** 368–70
- [23] Tran F and Blaha P 2009 Accurate band gaps of semiconductors and insulators with a semilocal exchange-correlation potential *Phys. Rev. Lett.* **102** 226401
- [24] Camargo-Martínez J A and Baquero R 2012 Performance of the modified Becke-Johnson potential for semiconductors *Phys. Rev. B* **86** 195106
- [25] Islam R, Cuono G, Nguyen N M, Noce C and Autieri C 2019 Topological transition in Pb_{1-x}Sn_xSe using meta-GGA exchange-correlation functional *Acta Phys. Pol. A* **136** 4
- [26] Goyal A, Gorai P, Toberer E and Stevanovic V 2017 *npj Comput. Mater.* **3** 42
- [27] Autieri C, Śliwa C, Islam R, Cuono G and Dietl T 2021 Momentum-resolved spin splitting in Mn-doped trivial CdTe and topological HgTe semiconductors *Phys. Rev. B* **103** 115209
- [28] Śliwa C, Autieri C, Majewski J A and Dietl T 2021 Superexchange dominates in magnetic topological insulators *Phys. Rev. B* **104** L220404
- [29] Islam R, Ghosh B, Cuono G, Lau A, Brzezicki W, Bansil A, Agarwal A, Singh B, Dietl T and Autieri C 2022 Topological states in superlattices of HgTe class of materials for engineering three-dimensional flat bands *Phys. Rev. Res.* **4** 023114
- [30] Silva J, Blas A and Hoat D 2019 Theoretical study of electronic and optical properties of antiferromagnetic β – MnS using the modified Becke-Johnson (mBJ) potential *J. Phys. Chem. Solids* **128** 310–5
- [31] Rauch T, Marques M A L and Botti S 2020 Local modified Becke-Johnson exchange-correlation potential for interfaces, surfaces and two-dimensional materials *J. Chem. Theory Comput.* **16** 2654–60
- [32] Yu M, Yang S, Wu C and Marom N 2020 Machine learning the Hubbard U parameter in DFT+ U using Bayesian optimization *npj Comput. Mater.* **6** 180
- [33] Vurgaftman I, Meyer J R and Ram-Mohan L R 2001 Band parameters for III–V compound semiconductors and their alloys *J. Appl. Phys.* **89** 5815–75
- [34] Shur M S 1996 *Handbook Series on Semiconductor Parameters* vol 1 (Singapore: World Scientific)
- [35] Chen A-B and Sher A 1995 *Semiconductor Alloys: Physics and Materials Engineering* (New York: Springer Science & Business Media)
- [36] Sohrabi L, Boochani A, Sebt S A and Elahi S M 2017 Structural, electronic and optical properties of InAs phases: by GGA-PBG and GGA-EV approximations *J. Chem. Res.* **41** 172–82
- [37] Philipp H and Ehrenreich H 1963 Optical properties of semiconductors *Phys. Rev.* **129** 1550
- [38] Ziane M I, Bensaad Z, Labdelli B and Bennacer H 2014 First-principles study of structural, electronic and optical properties of III-arsenide binary GaAs and InAs and III-nitrides binary GaN and InN: improved density-functional-theory study *Sens. Transducers* **27** 374
- [39] Aspnes D E and Studna A A 1983 Dielectric functions and optical parameters of Si, Ge, GaP, GaAs, GaSb, InP, InAs and InSb from 1.5 to 6.0 eV *Phys. Rev. B* **27** 985–1009
- [40] Namjoo S and Puschnig P 2022 Optical properties of InAs, InSb and InAs_xSb_{1-x} ($x=0.25, 0.5, 0.75$) alloys under strain *Comput. Condens. Matter* **30** e00610
- [41] Namjoo S, Rozatian A S H, Jabbari I and Puschnig P 2015 Optical study of narrow band gap InAs_xSb_{1-x} ($x=0, 0.25, 0.5, 0.75, 1$) alloys *Phys. Rev. B* **91** 205205
- [42] Smith D L and Mailhot C 1987 Proposal for strained type II superlattice infrared detectors *J. Appl. Phys.* **62** 2545–8
- [43] Manyk T, Michalczewski K, Murawski K, Martyniuk P and Rutkowski J 2019 InAs/InAsSb strain-balanced superlattices for longwave infrared detectors *Sensors* **19** 1907
- [44] Smith D L and Mailhot C 1990 Theory of semiconductor superlattice electronic structure *Rev. Mod. Phys.* **62** 173–234
- [45] Tsai T-Y, Michalczewski K, Martyniuk P, Wu C-H and Wu Y-R 2020 Application of localization landscape theory and the $k \cdot p$ model for direct modeling of carrier transport in a type II superlattice InAs/InAsSb photoconductor system *J. Appl. Phys.* **127** 033104
- [46] Kroemer H 2004 The 6.1 Å family InAs, GaSb, AlSb) and its heterostructures: a selective review *Physica E* **20** 196–203
- [47] Jiang M, Xiao H, Peng S, Qiao L, Yang G, Liu Z and Zu X 2020 Effects of stacking periodicity on the electronic and optical properties of GaAs/AlAs superlattice: a first-principles study *Sci. Rep.* **10** 1–7
- [48] Sajjad M, Singh N and Schwingschlögl U 2018 Strongly bound excitons in monolayer PtS₂ and PtSe₂ *Appl. Phys. Lett.* **112** 043101
- [49] Varrassi L, Liu P, Yavas Z E, Bokdam M, Kresse G and Franchini C 2021 Optical and excitonic properties of transition metal oxide perovskites by the Bethe-Salpeter equation *Phys. Rev. Mater.* **5** 074601
- [50] Reining L 2016 Linear response and more: the Bethe-Salpeter equation *Quantum Materials: Experiments and Theory (Modeling and Simulation* vol 6) ed E Pavarini, E Koch, J van den Brink and G Sawatzky (Forschungszentrum Jülich) ch 10 (available at: www.cond-mat.de/events/correl16)
- [51] Sottile F 2003 Response functions of semiconductors and insulators: from the Bethe-Salpeter equation to time-dependent density functional theory *PhD Thesis* Ecole Polytechnique X